

LA-8412-MS

*Q-1633*

Informal Report

*201  
8/13/80  
T.S.*

**MASTER**

**Industrial Applications of Computed Tomography at  
Los Alamos Scientific Laboratory**

University of California



**LOS ALAMOS SCIENTIFIC LABORATORY**

Post Office Box 1663 Los Alamos, New Mexico 87545

INDUSTRIAL APPLICATIONS OF COMPUTED TOMOGRAPHY  
AT LOS ALAMOS SCIENTIFIC LABORATORY

by

R. P. Kruger, R. A. Morris, G. W. Wecksung, G. Wonn, R. London

ABSTRACT

A research and development program was begun two years ago at the Los Alamos Scientific Laboratory (LASL) to study nonmedical applications of computed tomography. This program had several goals. The first goal was to develop the necessary reconstruction algorithms to accurately reconstruct cross sections of nonmedical industrial objects. The second goal was to be able to perform extensive tomographic simulations to determine the efficacy of tomographic reconstruction with a variety of hardware configurations. The final goal was to construct an inexpensive industrial prototype scanner with a high degree of design flexibility. This report describes the implementation of these program goals.

---

I. INTRODUCTION

Computed transverse axial tomography has been applied to such diverse disciplines as electron microscopy,<sup>1</sup> radio astronomy,<sup>2</sup> and most notably nuclear medicine,<sup>3</sup> and medical radiology.<sup>4-6</sup> Its introduction in the latter instance has provided a new dimension for that discipline. As the word implies, tomography produces an image of a cross section slice through an object as opposed to the conventional single x-ray view or projection of that object. Projections at several angles are used to reconstruct the tomographic cross sections. The ability to image cross-sectional slices through anatomy without obstruction from over- or underlying features has proven invaluable in medicine.

Boundary detection and surface reconstruction from several adjacent cross sections soon may also have a similar impact on medical diagnosis.<sup>7</sup> However, the applicability of these technologies to industrial inspection and nondestructive testing are just beginning to be explored.<sup>8-12</sup> Possible reasons for this

relative lack of industrial applications are the present high cost of commercial scanners, uncertainty as to which type of x-ray source/detector to use for a given application, and the cumbersome physical equipment configurations that may sometimes be necessary. Also, as with all new techniques, there is a learning period that potential users must initially undertake. If the specific inspection task is not time or sensitivity critical, the first reason is largely eliminated since film can be used as the image recording medium. This film record can then be analyzed off-line at a later time. However, the use of film has several disadvantages. First, film has a shorter dynamic range than solid-state x-ray detectors. Secondly, the relatively uncollimated nature of normal cone beam x-ray exposures will yield higher levels of scattered radiation with a corresponding loss of image contrast and material density information.

The first limitation is inherent to film as a medium and cannot be avoided. Proper shielding of the film cassette can, however, reduce scattered radiation. In addition, multiple slit image recordings of all necessary tomographic projections on one or a very few sheets of radiographic film is also possible. This will not only reduce scattering onto the film, but will effectively reduce the cone beam of radiation from the source to a fan beam of known solid angle. The latter diverging ray problem is easily corrected as will be demonstrated later.

Film possesses one attribute that may make it useful in some industrial environments where time or sensitivity are not critical. Its resolution is superior to even the most highly collimated detector. At the present time we hypothesize that the smallest practical collimator may have an open area of approximately 1 by  $10^4 \mu\text{m}^2$ . Film could exceed this resolution limit by two orders of magnitude.

A significant advantage when using tomography in many industrial applications is the large difference in attenuation coefficient ( $\mu$ ) between various materials. For instance, an air void surrounded by a background of a heavy metal is much easier to detect with fewer penetrating photons than tissue types that exhibit similar attenuation coefficients.

Thus, these high-attenuation differentials can yield detectable defects with comparatively rapid but high-resolution scans using a properly collimated solid state detector. The performance trade-offs appear to be cross section resolution, material attenuation differentials, and projection gathering time.

A collimated detector is a more efficient, i.e., more sensitive, recorder of available photons. However, as the collimator open area is reduced, fewer photons can be recorded in a given interval of time. Also, as has been mentioned, practical sizes of detector collimation cannot match the resolution of film for realistic source strengths.

While it was mentioned earlier that these trade-offs could limit the industrial applicability of computed tomography, this limitation can also be overcome. It is possible through experimentation and computer simulations to determine the optimal practical choice of the source intensity and energy range as well as the choice of a matching detector medium. Computer simulation will then determine the expected image quality with these choices along with the flexible, but finite, time constraint placed on the gathering of the necessary projections. The tomography simulations to follow were computed with these considerations in mind. The modularity of the tomographic device under development will allow the flexibility to make a wide range of possible hardware configurations realizable.

## II. TOMOGRAPHIC RECONSTRUCTION FROM PROJECTIONS

Figure 1 depicts in symbolic form the scanning and reconstruction process using three projections  $p(t, \theta_i)$  for  $i = 1, 2, 3$ . However, the number of projections can vary between 2 and 360 in presently known applications. Each projection  $p(t, \theta)$  is essentially a line integral along a path  $L$  through the object cross section relative to an angle  $\theta$ . In fact, if  $f_z(x, y)$  denotes the object absorption density at a given  $z$ -axis height, we have

$$I(t, \theta) = I_0(t) e^{-p(t, \theta)} \quad , \quad (1a)$$

where  $I_0$  and  $I$  are incident and transmitted x-ray intensities, respectively, and

$$p(t, \theta) = \int_L f_z(t \cos \theta - s \sin \theta, t \sin \theta + s \cos \theta) ds \quad . \quad (1b)$$

Thus, if  $I_0(t)$  and  $I(t, \theta)$  are measured, then

$$p(t, \theta) = -\ln [I(t, \theta)/I_0(t)] \quad (1c)$$

is known.

The set of projections, once obtained, are available for the reconstruction process. Several algorithms have been proposed for the reconstruction task. Iterative approaches appear to have some merit when a very limited number of projections are available.<sup>13,14</sup> It is felt that the industrial environment will not often be constrained by this limitation. It has been our experience that when more than 30 projections are available over at least 180 degrees of rotation, the filtered back projection algorithm<sup>15</sup> performs satisfactorily. It is also a comparatively simple algorithm that has been implemented in hardware in several medical systems. For these reasons it was chosen for our initial work. The basis of this method will now be discussed. The case where  $t$  and  $\theta$  are both continuous will be initially considered.

The one-dimensional Fourier transform of a projection  $p(t,\theta)$  is  $P_\theta(v)$  defined

$$P_\theta(v) = \int_{-\infty}^{\infty} p(t,\theta) e^{-j2\pi vt} dt \quad , \quad (2)$$

where  $v$  is measured as a spatial frequency. If  $P$  is filtered with a frequency domain ramp or rho filter  $|v|$  and inverse-transformed, this will produce a filtered projection  $\tilde{p}(t,\theta)$  defined

$$\tilde{p}(t,\theta) = \int_{-\infty}^{\infty} P_\theta(v) \cdot |v| \cdot e^{j2\pi vt} dv \quad . \quad (3)$$

The rho filter effectively produces the phaseless derivative  $\tilde{p}(t,\theta)$  of the original projection. Using these filtered projections, the cross section  $f_z(x,y)$  at a given  $z$ -axis height can be reconstructed exactly using

$$f_z(x,y) = \int_0^\pi \tilde{p}(x \cos \theta + y \sin \theta, \theta) d\theta \quad . \quad (4)$$

However, exact reconstruction is not possible since the number of angles  $\theta$  at which projections are actually collected is always discrete and finite. Also,  $p(t,\theta)$  is usually a sampled or digitized waveform. Thus, for finite  $\theta$  denoted  $\theta_i$ , the reconstruction can be approximated by

$$f_z(x,y) = \frac{\pi}{K} \sum_{i=1}^K \tilde{p}(x \cos \theta_i + y \sin \theta_i, \theta_i) \quad . \quad (5)$$

It should also be noted that the mathematically exact rho filter  $|v|$  is often modified in many applications. The use of a low-pass filter to attenuate noise-dominated higher frequencies is often used in conjunction with the rho filter in these instances.

The reconstruction algorithm just discussed assumes that the projection data was gathered from parallel rays. This would be the case when projections are collected using a single collimated detector. However, the use of several collimated detectors positioned on an arc defined by a fan beam angle  $\alpha$  yields nonparallel ray projection data. This latter fan beam geometry is used because it greatly accelerates the projection-gathering process and is a more efficient use of the x-ray source flux. Thus, the fan beam projection rays must be converted to the equivalent set of parallel projection rays before reconstruction is undertaken.

### III. FAN BEAM GEOMETRY CORRECTION

The problem of converting fan-beam data to parallel-beam data in computer-aided tomography is often referred to as the "sorting problem," since each data point collected on a fan-beam projection corresponds to some data point on a parallel-beam projection taken at a different rotation angle.<sup>16</sup> Also, since the data is discrete, a two-dimensional interpolation is required. Such a conversion permits reconstruction by standard algorithms that operate on parallel-beam data. This approach has been criticized by Horn<sup>17</sup> as not very effective since the accuracy is compromised by the interpolation step, especially in the case of noisy data.

In this paper, we consider the "sorting problem" as a simple two-dimensional rubber sheet transformation between the fan-beam and parallel-beam sinograms. Although the interpolation step is unavoidable, we find that it contributes to a noise reduction in the converted parallel-beam sinogram over a genuine parallel-beam sinogram, when the noise levels in the collected data are the same and exceed the interpolation error.

The geometry for fan-beam data collection is presented in Fig. 2. Here the object is enclosed in a circle of radius  $R$  centered at the origin  $O$  of the  $x'-y'$  scanner coordinate system. The fan angle of the x-ray source is  $\alpha$ . The  $x-y$  axis is fixed in the object that rotates about  $O$ . For each rotation angle  $\theta'$ , a projection  $h(x',\theta')$  from the point source  $S$  located at a distance  $D$  on the

$y'$  axis above 0 can be recorded. Indeed, the value of  $h(x',\theta')$  is just the line integral along the ray SP. Here  $x'$  is the intercept along the  $x'$ -axis by the ray.

Moreover, if we consider the ray SP as a ray from a parallel-beam projection, then from inspection of Fig. 2 we see the rotation angle  $\theta$  would be  $\theta' - \phi$ , and the projection point would be offset a distance  $t$  from the origin. Here  $\phi$  is the angle between SP and  $y'$ -axis, and  $t$  is the normal distance of SP from the origin in the fan-beam geometry. Thus, if  $p(t,\theta)$ ,  $-R \leq t \leq R$ , denotes parallel-beam projection data taken at a rotation angle  $\theta$ , we can write for the ray SP

$$h(x',\theta') = p(t, \theta' - \phi) \quad . \quad (6)$$

From Fig. 2, we observe

$$\sin \phi = t/D, \text{ and} \quad (7)$$

$$\cos \phi = t/x' \quad . \quad (8)$$

Combining the above equations, we find that in general<sup>18</sup>

$$p(t,\theta) = h \left( \frac{t}{\sqrt{1 - (t/D)^2}}, \theta + \sin^{-1}(t/D) \right) \quad . \quad (9)$$

The function  $p(t,\theta)$  is often called a sinogram since, as a function of two variables, it can be displayed as a picture in which point objects appear as sinusoidal curves. If we call  $h(x',\theta)$  the fan-beam sinogram, then the coordinate transformation of Eq. (9)

$$\left\{ \begin{array}{l} x' = \frac{t}{\sqrt{1 - (t/D)^2}} \\ \theta' = \theta + \sin^{-1}(t/D) \end{array} \right. \quad - R \leq t \leq R \quad (10)$$

defines a rubber-sheet (one-to-one and continuous) transformation from the parallel-beam sinogram to the fan-beam sinogram. This transformation has the

interesting property that parallel-beam projection data  $p(t, \theta)$  taken at a fixed rotation angle  $\theta'$  depend only on fan-beam data for rotation angles  $\theta$  with

$$\theta - \sin^{-1}(R/D) \leq \theta' \leq \theta + \sin^{-1}(R/D) \quad . \quad (11)$$

From Fig. 2 we see that

$$\alpha = 2 \sin^{-1}(R/D) \quad (12)$$

is just the angle subtended by the object at the point source S. Parallel-beam projections have the well-known property

$$p(t, \pi + \theta) = p(-t, \theta) \quad . \quad (13)$$

Thus, projection data need only be collected over 180° of rotation for complete reconstruction. However, this is not the case for fan-beam projections, since magnification is introduced. From Eqs. (11) and (12), we see that fan-beam projections must be collected over the range  $-\alpha/2 \leq \theta' \leq \pi + \alpha/2$  of rotation angles  $\theta'$  in order to derive parallel-beam projections over the range  $0 \leq \theta \leq \pi$  of rotation angles  $\theta$ , an increase by  $\alpha$ , the angle of the fan-beam subtended by the object.

As in the reconstruction process presented earlier, it is necessary for reconstruction purposes to obtain the discretized sinogram of parallel-beam data  $p(t_i, \theta_j)$  equally spaced in both  $t$  and  $\theta$ , i.e.,

$$\begin{aligned} t_i &= i \cdot \delta t, \quad i = -N_1, \dots, N_1 \quad , \\ \theta_j &= j \cdot \delta \theta, \quad j = -N_2, \dots, N_2 \quad , \end{aligned} \quad (14)$$

for suitable  $\delta t$ ,  $\delta \theta$ ,  $N_1$ , and  $N_2$ . Unfortunately, substitution of the sample positions given by Eq. (14) into the transformation Eq. (10) produces unequally spaced values of  $x'$  and  $\theta'$ . Since the fan-beam data is usually sampled in a regular manner, i.e.,  $\theta'$  equally spaced and either  $x'$  or  $\phi$  equally spaced, a two-dimensional interpolation is necessary.



In general, the image  $(x'_{ij}, \theta'_{ij})$  of the parallel-beam sample point  $(t_i, \theta_j)$  will lie in the interior of a rectangle with vertices located at fan-beam sample positions, i.e.,

$$\begin{aligned} x'_k &\leq x'_{ij} \leq x'_{k+1} , \\ \theta'_\ell &\leq \theta'_{ij} \leq \theta'_{\ell+1} , \end{aligned} \tag{15}$$

for appropriate sample indices  $k, \ell$ .

We use bilinear interpolation to get

$$\begin{aligned} h(x'_{ij}, \theta'_{ij}) &\approx w_1 h(x'_k, \theta'_\ell) + w_2 h(x'_{k+1}, \theta'_\ell) \\ &+ w_3 h(x'_k, \theta'_{\ell+1}) + w_4 h(x'_{k+1}, \theta'_{\ell+1}) , \end{aligned} \tag{16}$$

where the weights  $w_1, \dots, w_4$  are selected so that  $h(x'_{ij}, \theta'_{ij}) = h(x'_\mu, \theta'_\nu)$  when  $(x'_{ij}, \theta'_{ij})$  coincides with each of the four vertex points  $(x'_\mu, \theta'_\nu)$ . Thus, it is reasonable to expect a small interpolation error when  $(x'_{ij}, \theta'_{ij})$  lies near the center of the rectangle.

We have noticed in computer simulations to follow that significant noise reduction in converting fan-beam data to parallel-beam equivalents can be achieved. A probable explanation of this observation follows. First of all, the noise is modeled as a signal-dependent Poisson type in which the noise variance is related to the signal. In the bilinear interpolation step, we need only consider noise values  $X_1, \dots, X_4$  at the vertices  $(x'_k, \theta'_\ell)$ ,  $(x'_{k+1}, \theta'_\ell)$ ,  $(x'_k, \theta'_{\ell+1})$ ,  $(x'_{k+1}, \theta'_{\ell+1})$ , respectively. Since the signal at the four vertices is roughly the same magnitude, we assume the noise to be additive with zero mean and variance  $\sigma^2$  dependent on the average signal at the vertices. Thus, by superposition we can consider the bilinear interpolation of the noise separately from the signal in which we claim there is a noise reduction effect. The interpolated noise  $Y$  can be expressed as

$$Y = w_1 X_1 + w_2 X_2 + w_3 X_3 + w_4 X_4 , \tag{17}$$

where the weights  $w_1, \dots, w_4$  are defined previously. We further assume that noise values at the vertices are independent. In this case we find that  $Y$  has

an average value of zero and has a variance,

$$\sigma_Y^2 = \sigma^2 \sum_{k=1}^4 w_k^2 . \quad (18)$$

One can verify that in bilinear interpolation the sum  $\sum_{k=1}^4 w_k^2$  is a quadratic function of the coordinates (taken separately) of the interpolation point that takes on a minimum equal to 1/4 at the center of the interpolation rectangle and assumes a value of unity at the vertex points. The behavior of the noise error is the reverse of that of the interpolation error, which leads to a balancing effect: near the center, interpolation error is large but noise error is small, while near a vertex the reverse is true. Obviously, when the noise standard deviation is much greater than the interpolation error, the bilinear interpolation step is a significant aid to the reconstruction by reducing noise. In the following computer simulation involving fan-beam conversion, the standard deviation of the noise in the interpolated parallel-beam data was reduced by a factor of 2/3 of that of genuine parallel-beam data, using the same noise parameters.

#### IV. SIMULATION STUDIES

We have found it beneficial to model proposed tomographic hardware configurations through computer simulations. The critical variables are the x-ray source flux strength and the energy range of the source. Sources may be of two types. First one can assume that the source of flux is monoenergetic or broad band. Cobalt 60 is an example of the former, while conventional bremsstrahlung or neutron sources are examples of the latter. We will treat each class of simulation with separate examples.

The basic inputs needed for the computer simulation in the monoenergetic case include the x-ray attenuation coefficient  $\mu$  of all materials at a specified radiation energy, the number of incident photons ( $I_0$ ) impinging on the detector per projection point  $p$  in a given time interval through an aperture size ( $m$ ), the number of pixels/projection ( $M$ ), and the number of projections  $w$  per reconstruction plane. Typically one is given experimentally derived values of  $\mu$  and  $I_0$ . An effective noiseless path length  $\bar{p}(t, \theta)$  through the phantom is then computed. Often the computation of each total path length through the object involves a random selection of individual discrete  $\mu$  bins along the chord length

being accumulated. A monoenergetic source spectrum  $S(E) = \delta(E)$  will be initially assumed. This yields a constant estimate of all  $\mu$  coefficients. Once  $\mu$  is estimated, this, along with the incident number of source photons  $I_0$ , is used to compute the standard deviation  $\sigma_p$  of each projection point. (See Appendix A.)

$$\sigma_p = \left( \frac{e \bar{p}}{I_0} \right)^{1/2} . \quad (19)$$

This is used to add signal-dependent Gaussian noise to each noiseless projection point of each  $w$  projection used in the simulated reconstruction. Thus, the noisy projection is

$$p_i(r) = \bar{p}_i(r) + \sigma_{p_i}(r) \eta , \quad (20)$$

where  $\eta(0,1)$  represents a random number from a Gaussian source with zero mean, and variance 1 and  $\bar{p}$  represent the noiseless projection.

Hanson<sup>19,20</sup> has verified that the threshold of detectability expressed as a signal-to-noise ratio (SNR) can be expressed as

$$\text{SNR} = \frac{\delta\mu}{\sigma_R} . \quad (21)$$

The standard deviation ( $\sigma_R$ ) of the noise of a tomographic reconstruction in a region of uniform  $\mu$  is

$$\sigma_R = \frac{\sigma_p}{\sqrt{w} m} K . \quad (22)$$

Values of SNR of between 2 and 5 with  $K = 0.5$  have been shown to allow a 50% detection probability of small (4-pixel area) air voids in heavy metals.

As an example, let us tomographically reconstruct a simulated 24-mm diam plutonium cylinder with  $w = 180$  evenly spaced projections over  $\theta = 180^\circ$ . There will be  $M = 256$  pixels/projection, a  $m = 0.1$  mm-square aperture, a 1-MeV  $^{60}\text{Co}$  source, and the  $\mu$  of plutonium will equal  $0.16 \text{ mm}^{-1}$ . Within the cylinder are eight circular air voids ( $\mu = 0$ ) ranging in diameter from 0.2 mm to 2.4 mm. Since  $\sigma_p$  is signal-dependent, we will estimate the maximum number of incident photons ( $I_0$ ) per aperture needed to produce a reconstruction with a minimum SNR of 4. This will yield a reconstruction where the smallest air void will be just

above the 50% perceptibility.

$$\sigma_R = \frac{\mu}{\text{SNR}} = \frac{0.16}{4} = 0.04 \quad (23a)$$

$$\max \sigma_p = \frac{\sigma_R \sqrt{w} m}{K} = \frac{(0.04)\sqrt{180} (.1)}{0.5} = 0.1073 \quad (23b)$$

$$\max \bar{p} = \int_G^{24} 0.16 \, dz = 3.84$$

$$\max I_0 = \frac{e^{\bar{p}}}{\sigma_p^2} = \frac{e^{3.84}}{(0.1073)^2} = 2546 \quad (23c)$$

$$\min I = I_0 e^{-\bar{p}} = 2546 e^{-3.84} = 55 \quad (23d)$$

Therefore, with  $I_0 = 2546$  incident photons, one should expect no fewer than  $I = 55$  exit photons incident on the x-ray detector. The  $\text{SNR} = 4$  should make 0.2-mm-diam air voids just detectable. Figure 3a shows the resultant 256 by 256 reconstruction  $f$ . The small void to the left of center is also quite detectable. The 0.2-mm void to the right of center is barely detectable, thus reinforcing the just-explained detection criteria. As a comparison, Fig. 3b shows the same phantom with an order of magnitude higher incident flux  $I_0$  and at least 2500 exit photons corresponding to a  $\text{SNR} = 10$ . As predicted, all voids are easily detected.

One further simulation has been undertaken. Once again the  $\text{SNR}$  was set at 4. This time, however, projection data was gathered by an ( $\alpha = 76^\circ$ ) fan beam of x-ray flux over 256 one-degree increments. The transformation previously explained converted these fan-beam projections into an equivalent set of parallel-beam projections. The reconstruction shown in Fig. 3c shows a perceived decrease in noise over that of Fig. 3a. One can speculate that the perceptibility detection threshold has been increased, i.e., the effective  $\text{SNR}$  has been increased in the latter case. From the computer simulation, using the same noise parameters, we found that the RMS error in the interpolated parallel-beam sinogram was 2/3 of the RMS error in the genuine parallel-beam sinogram. This implies a noise reduction of the same magnitude in the reconstruction domain from Eq. (22). The measured noise reduction factor was 0.525.

The second study is a tomographic simulation of a broad band spectral source and detector.<sup>10</sup> It involves a research project sponsored by the National Bureau of Standards (NBS) to assess the use of resonance-neutron computed tomography for the assay of fissile materials.

While this study involves neutron, rather than x-ray simulation, the algorithm developed could just as easily simulate an x-ray bremsstrahlung hardware configuration. It was the goal of this research to provide investigators at NBS with realistic simulations of expected tomographic reconstruction quality given the expected size of objects to be reconstructed, the resolution of the reconstruction, and the nature of the detectors to be used. These have been taken into consideration in the simulations that follow.

The simulations to be presented were used to assess the feasibility of using resonance-energy neutron beams to generate tomographic images of fissile materials. Since tomographic images are quantitative, the hypothesis to be tested was that of matching the detector to the material to be detected so that fissile material inside a closed container could be identified. For example, a  $^{235}\text{U}$  fission detector would be used to locate and identify the presence of all  $^{235}\text{U}$  in the container. The same procedure would be repeated for  $^{239}\text{Pu}$  and  $^{233}\text{U}$ .

A proposed NBS experimental apparatus is shown in Fig. 4. It consists of a neutron source and a thick variable-width source collimator designed to produce a pencil beam of primary neutrons for irradiation of a standard. The standard consists of a 23.6-cm-diam iron cylinder with various 1-cm-diam cylinders of fissile isotopes inside. The large cylinder will be mechanically moved and rotated to produce projection data with a parallel rather than a fan-beam radiation pattern. The detector collimator would be similar in design to that of the source collimator. The detectors will be sensitive to the fission cross sections for  $^{233}\text{U}$ ,  $^{235}\text{U}$ , and  $^{239}\text{Pu}$ .

The simulation that was performed was based on the following assumptions:

1. The materials were homogeneous and contained only a single nuclide.
2. The exponential absorption law holds.
3. The detectors were fission chambers and their response was proportional to the number of incident neutrons that underwent a fission reaction.

Figure 5 shows the total neutron cross sections ( $\mu$  values) used in this experiment. There were 38 discrete cross sections from .683 eV to 2 keV used to simulate the spectral continuum. The simulated tomographic detector(s)

consisted of fissile material(s) with known fission cross section(s) shown in Fig. 6. The detector records a number proportional to the number of transmitted neutrons that underwent a fission reaction in the detector. Each projection used in the reconstruction consisted of 128 points, and the projections were gathered over 180° ( $\theta = 1,180$ ). Each projection point was computed in the following manner. At each projection point,  $t$ , the neutron flux passing through the phantom was computed. The total neutron signal  $I_{\theta}(t)$  was recorded with different neutron detectors for each of the isotopes previously described.

The following formula summarizes this accumulation:

$$I_{\theta}(t) = \sum_{E=1}^{38} I(E) \cdot D_K(E) \cdot e^{-(\mu_{\theta}(E,t))} \quad (24)$$

for  $t = 1,128$

where  $\theta = 1,180$        $K = 1,3$ .

$I$  is the number of neutrons emitted by the source per energy group  $E$ .

$D_K$  is the fission detector sensitivity to a specific isotope ( $K$ ) as a function of energy bin  $E$ .

$\mu_{\theta}$  is the integrated neutron pathlength through the phantom at projection point  $t$ , angle  $\theta$ , and energy group  $E$ . The total neutron cross sections used to compute these  $\mu$  are shown in Fig. 5.

Each of three detector responses  $D$  was computed as a function of energy group  $E$  as follows:

$$D_K(E) = 1 - e^{-F_K(E) \cdot x} \quad \begin{matrix} E = 1,38 \\ K = 1,3 \end{matrix} \quad (25)$$

where  $F_K(E)$  is the fission cross section of each isotope ( $K$ ) as shown in Fig. 6, and  $x$  is the assumed fission detector thickness (1 mm). Each total detected signal  $I_{\theta}(t)$  was then converted to total neutron pathlength  $p(t,\theta)$  by the following equation:

$$p(t,\theta) = \ln(I_0/I_{\theta}(t)) \quad (26)$$

for  $t = 1,128$ ;  $\theta = 1,180$  ,

where  $I_0$  represents the sum of all source neutrons  $I(E)$  over the total energy spectrum.

Poisson noise was added to each projection point  $I_\theta(t)$  prior to the use of Eq. (26) to simulate neutron noise characteristics. (See Appendix B.) These operations were repeated for each of the 180 projections mentioned earlier. In order to determine the sensitivity of the phantom to each of three separate fission detectors,  $D_k(E)$  was successively replaced, and the projection formation repeated.

The reconstruction of the noisy projections was then undertaken for each detector. Each projection was filtered using a filter with the following frequency domain response prior to back projection:

$$H(f) = f \quad ; \quad 0 \leq f \leq f_n/4 \tag{27}$$

$$= \frac{f_n}{8} \left[ 1 + \cos \left( 4\pi(f - f_n/4) / 3f_n \right) \right] ; \quad f_n/4 \leq f \leq f_n .$$

The Nyquist frequency  $f_n$  is 0.27 pixels/mm in these simulations. The first half of Eq. (27) is the analytically exact phaseless differentiator used in the original back projection algorithm first derived by Radon.<sup>15</sup> The modification represented by a Hanning roll-off in the second half of the equation is necessary to reduce ringing artifacts and the effects of noise. The ringing artifacts are present in the reconstructions at material boundaries of high contrast such as exist between these dense fissile materials and air. These filtered projections were used to reconstruct the tomographic cross sections using the back projection algorithm.

Figures 7a, 7b, and 7c show typical reconstructions. These reconstructions were created with the fission detectors sensitive to each of the fissionable materials as described earlier. In each figure, the  $^{233}\text{U}$  cylinder is shown centered at pixel (64,64) in the 128 by 128 reconstruction plane. Each pixel represents a 1.85-mm-square area. The  $^{235}\text{U}$  and  $^{239}\text{Pu}$  cylinders are shown to the right of and below the  $^{233}\text{U}$  cylinder, respectively. Table 1 is a matrix that shows the peak amplitude of the responses of each cylinder as a function of the chosen detector.

These simulations indicate that differentiation of fissionable materials by neutron tomography can be successful. Nondestructive quantitative assays of

TABLE I  
VARIOUS RESPONSE PEAKS

Detector Type	Peak Response		
	$^{233}\text{U}$	$^{235}\text{U}$	$^{239}\text{Pu}$
$^{233}\text{U}$	.312	.240	.193
$^{235}\text{U}$	.264	.264	.201
$^{239}\text{Pu}$	.288	.264	.265

sealed radioactive containers may be possible using this technique. The code developed in this research can be used in simulations where it is desirable to model broadband spectral source and detector configurations.

#### V. BEAM-HARDENING CORRECTION

The simulations previously discussed do not include degradations in reconstruction quality that can be caused by the so-called "beam-hardening" effect. This will be used as a generic term to describe changes in effective beam energy ( $E$ ) as material densities are traversed.

The linear attenuation coefficients ( $\mu$ ) of all materials are a function of beam energy ( $E$ ). If the object to be reconstructed were irradiated with a source spectrum  $I_0(E_0)$  of monochromatic photons, then  $I_0(E_0) = I_0 \delta(E - E_0)$  where  $\delta$  denotes a unit impulse of intensity  $I_0$ . Cobalt 60 has two such impulses quite near 1200 keV. Iridium 192 has several such peaks and a mean energy of 390 keV. A typical x-ray source has a maximum energy of about 400 keV with a mean energy around 300 keV. These three sources have a decreasing degree of monochromaticity of their source spectrum. Since lower energy photons are absorbed more than those of higher energies and higher energy photons tend to be scattered to a lower energy, the effective energy of the source changes as the object is penetrated. In the former case, the mean source beam energy increases with a corresponding decrease in effective  $\mu$  as a material is progressively penetrated. This is classic beam hardening. In the latter case, the mean beam energy decreases and the effective  $\mu$  increases. This describes a "softening" of the radiation. Beam softening can be eliminated with good collimation and/or energy discrimination. Scanning around the object results in an energy averaging



effect from Eq. (5). This reduces but does not eliminate the hardening problem. The resulting visual effect is a "cupping artifact," which will be demonstrated in the experimental work on defect detection in reactor pipe cross sections.

A streaking artifact occurs when the object to be reconstructed is rectangular rather than circular. This will also be demonstrated. As before, let  $I(E)$  denote a polychromatic x-ray or gamma-ray source beam. If these photons are detected with a perfect detector, the integrated signal is

$$I_0 = \int_0^{\epsilon} I(E) dE \quad , \quad (28)$$

where  $\epsilon$  denotes the maximum energy present in the beam. If the source beam passes through a cross section of an object with linear attenuation coefficient  $\mu(x,y,E)$ , the detected signal intensity will be

$$I_{\theta}(x) = \int_0^{\epsilon} I(E) \exp \left[ - \int_L \mu(x,y,E) dy \right] dE \quad , \quad (29)$$

as in Eqs. (1) and (24), the polychromatic projection pathlength is defined

$$p(x,\theta) = \ln \left[ I_0 / I_{\theta}(x) \right] \quad . \quad (30)$$

When beam changes occur,  $\mu$  changes as a function of  $x$  and  $y$  as a result of changes in beam energy ( $E$ ).

If the source is monochromatic [ $I_0(E_0) = I_0 \delta(E - E_0)$ ] and efforts are made to eliminate beam softening, Eq. (30) reduces to

$$p(x,\theta) = \int_L \mu(x,y,E_0) dy \quad , \quad (31)$$

and the projection data represents the integrated path length  $L$  through the object at angle  $\theta$  for a single energy  $E_0$ . Beam energy does not change, and  $\mu$  remains constant as a result.

A rather simple correction for beam hardening is possible when the object being irradiated is composed of a single material. In this case, one approach could be to create a physical step or wedge phantom of this material. The object when irradiated would yield measured intensities  $I$  as a function of physical

thickness  $x$ . A curve of  $x$  (ordinate) vs  $p(x,\theta)$  (abscissa) could be fit to an  $n^{\text{th}}$  order polynomial. The corrected projection  $p_c$  would be

$$p_c = p_c(x,\theta) = \sum_{i=1}^n a_i p(x,\theta)^i \quad . \quad (32)$$

The corrected projections are then used to reconstruct the tomographic cross section.

In practice,  $n = 2$  is often used since classic hardening will follow an approximately quadratic path. This correction technique will be applied in the experimental section of the report.

When the object is composed of more than one material density, the situation becomes more complex since an  $n^{\text{th}}$  order polynomial estimator must be found for each material present in the object. The following is an approach that we feel could be successful. Let us assume materials zirconium (Z) and uranium oxide (UO) are present in our object. First, an initial tomographic reconstruction is completed. This reconstruction has artifacts, but it is possible to isolate the uranium oxide by interactively selecting a gray level threshold above which only uranium is visible on the screen of our display. (Such a thresholding operation for separating zirconium and hafnium in a test piece will be demonstrated later.) Next, the value of the length  $x_u$  of uranium is plotted vs the average  $P_u$  value along the path. This step is repeated for each bin of each projection. The resulting scattergram is fitted to an  $n^{\text{th}}$  order polynomial. The zirconium path lengths  $x_z$  are similarly plotted. The corrected total path-length  $x = x_z + x_v$  is the sum of the two

$$p(x,\theta) = p_c(x_z,\theta) + p_c(x_v,\theta) \quad (33)$$

$$p_c(x,\theta) = \sum_{i=1}^{n_z} a_i p(x_z,\theta)^i + \sum_{i=1}^{n_u} \alpha_i p(x_u,\theta)^i \quad , \quad (34)$$

where  $n_z = n_u = 2$  will probably suffice.

It is clear that this technique can be extended beyond the case where two materials are present as long as adequate thresholds can be found that isolate the various materials. The cost of this approach is an additional reconstruction.

In the experimental work to follow, only the single material method was implemented by a computer algorithm. In addition, a special phantom was not constructed to estimate an  $x$  vs  $p$  curve. Instead, the geometrical path  $x$  through the actual objects under study were computed and matched to the detector response  $p$  at the corresponding point. The resulting scattergram of  $x$  vs  $p$  was fit to a quadratic curve in order to find the  $a_i$  correction coefficients. The correction procedure was applied to round test objects only. These objects included an aluminum test piece with various size holes drilled in it, and several sized reactor pipes with either real or programmed defects in their walls. In all these cases a master uncorrected projection  $p$  was computed by averaging the individual real projections each synchronized to a common point such as the point of maximum wall thickness. This was possible because of the rounded nature of these objects. The geometrical pathlengths  $x$  through the material were also easily computed because of the circular shape. This correction process worked surprising well and did not require the construction of a separate wedge or step phantom. The examples that follow will demonstrate the success of this relatively simple correction procedure.

## VI. FILM-BASED TOMOGRAPHY

Film can be used as a substitute for an electronic detector or detector array when sensitivity and projection-gathering time can be successfully traded-off with resolution. Several examples of film-based tomography will demonstrate this.

A study was conducted to determine the possibility of detecting and sizing cracks in reactor cooling water tubes. The tomographic inspection will, in turn, be used by Batelle Northwest Laboratory to calibrate eddy current inspection of these tubes. The cracks occur on the outside diameter of the nominal 1.2-mm-thick wall tube and generally run with the tube axis in the plane of the crack. The cracks vary in depth and width, but are all less than 0.1-mm wide and have a maximum depth equal to the wall thickness (1.2mm). The outside diameter of the tubing is 22 mm.

Because the cracks to be visualized are very small ( $< 0.1$  mm by 1 mm) with high x-ray absorption contrast, industrial x-ray film was chosen as the detector. While the film has relatively low dynamic range, it has excellent spatial resolution comparable to a collimated nuclear detector. Figure 8 illustrates the equipment. The 4-mm radiation gap projects to 4.7 mm on the film. This requires

that the film translate 5.7 mm between exposures to prevent double exposures. The x-ray source was shielded with lead bricks with a small port to collimate or at least minimize the stray scattered radiation.

After each exposure, the tube was rotated  $1^\circ$  and the film advanced 5.7 mm. The movement of the film was digitally controlled by the mechanical transport subsystem of the prototype scanner to be discussed in the next section. The fiducial plate was mounted on the back of the upper exposure slit plate and served as a reference mark for the subsequent microdensitometer scanning. To permit the fan-beam geometry to be corrected to the normal parallel beam geometry, views were taken from  $-10$  to  $190^\circ$ .

After the slit images were developed, each was scanned with a scanning microdensitometer using a  $100\text{-}\mu\text{m}$  by  $1500\text{-}\mu\text{m}$  slit. The  $100\text{-}\mu\text{m}$  dimension was parallel to the scanning direction. The digital data resulting from each scan was stored on magnetic tape prior to reconstruction in the computer. The scans were aligned by referencing the start of each scan to the fixed fiducial image. A sinogram of the pipe is shown in Fig. 9.

Figure 10 illustrates the correlation between the visible cracks using an unwrapped mosaic of the pipe's surface and the cracks detected in the reconstruction. The most important conclusions we can draw at this point are

- 1) Many of the cracks in the pipe are detected by tomography.
- 2) The crack indications visible in the reconstruction appear to have structure (shape and orientation).

The cracks appear blurred for several reasons. Cracks do not run perfectly linear with the pipe axis but are somewhat irregular. Since the microdensitometer slit is 1.5-mm long, this in effect integrates along the slit length producing a wider crack image and a lower contrast image. Secondly, the finite scanning slit width ( $100\ \mu$ ) introduces its own blur factor that must be accounted for. Similar applications will be undertaken later with an electronic detector.

## VII. REIMBURSABLES

We will briefly describe a second film-based application undertaken by LASL for Westinghouse-Hanford. This resulted in a tomographic analysis of a spent X-229-A fuel rod bundle using the filtered backprojection and maximum entropy reconstruction algorithms.

The input data consisted of 18 transmission neutron radiographs supplied by Westinghouse-Hanford. Each radiograph consisted of a 13-in length of fuel bundle containing 61 circular pins in a hexagonal matrix clad. Figure 11 is an example of three of the radiographs at 0°, 30°, and 60°.

While the quality of these radiographs was extraordinary, there were no fiducials on the films to provide registration between films. With the help of Hanford personnel, we manually provided these fiducials. Each radiograph was scanned from the base to the apex. Twelve such scans were undertaken at approximately 1-in intervals up the fuel assembly. The scan aperture was a rectangular slit that was 100- $\mu$  wide and 1500- $\mu$  high. Thus, the resolution of each projection was 100  $\mu$ , and the reconstruction plane had a depth of 1.5 mm.

The 12 scans for each angular view and 18 views over 180° were used as the basis for reconstruction. For example, if one were to choose the sixth scan line from the bottom in each of the 18 views, these 18 projections would constitute the input to the reconstruction algorithm. The output would be a cross-sectional reconstruction of a 1.5-mm-thick plane half way up the bundle. One additional limitation of the input data should be mentioned. The radiographs were exposed with a cone beam of neutron flux. As a result, some spatial distortions occurred, especially near the base and the apex. These distortions caused those reconstructions to be inaccurate in these regions, since the reconstruction algorithms used require coplanar data. While it is easy to correct for a fan beam of radiation in tomography, the same cannot yet be practically said for a cone beam of radiation. For these reasons, we expected the data near the central plane (plane 6) to yield the best reconstructions in this case. The film recorded data was proportional to  $I_{\theta}$  or total neutron intensity. Each total detected signal  $I_{\theta}$  can then be converted to total neutron pathlength  $p(t,\theta)$  by Eq. 26. It should be noted that  $I_{\theta}$  is also corrupted by Poisson counting and film noise, beam scatter, film nonlinearities, and probable beam hardening.

This work assumed that  $I_0$  represented the recorded film density of the background (BG) air pathlength between the source and the film. This background density was recorded in specular density units on our scanning microdensitometer. The film recorded neutron intensity through the object was  $I_{\theta}$ . The projection data  $p$  used in the reconstructions was

$$p(t, \theta) = \ln(BG/D)$$

$$t = 1,800 \quad \theta = 1,180,10 \quad , \quad (35)$$

where D was the microdensitometer-recorded film density.

Next the 800 points in each projection were averaged down to 400. This was done because there was excessive projection resolution given the number of projections available. To estimate the background density, a straight line interpolant was used between projection points 5 and 396 for each projection. This also partially corrected for observed background bias changes probably due to misalignment of the source beam center.

The maximum entropy reconstruction technique also set projection points  $i = 1, \dots, 4$  and  $i = 397, 800$  to 0. This helped to suppress background artifacts. Both backprojection and maximum entropy reconstruction algorithms<sup>21</sup> were used to analyze this data. However, a detailed discussion of the maximum entropy method is beyond the scope of this report. It is felt that filtered backprojection is of marginal utility for the number of views present in this application. The second reconstruction algorithm to be used is an iterative method involving the maximization of entropy. It is designed to optimize the reconstruction when relatively few projections are obtainable.

Figure 12 is a 400 by 400 pixel reconstruction of the fuel bundle at plane 6 using backprojection. One should note that while the reconstruction is sharp, there are numerous background artifacts present. However, in spite of artifacts, the hollow pin centers indicative of a spent assembly are clearly visible.

Figure 13 is plane 6 reconstructed with maximum entropy using eight iterations. Compared to the convolutional reconstruction, the maximum entropy reconstruction has the following advantages:

- 1) Ringing artifacts are suppressed outside the hexagon.
- 2) The circular shape of the fuel pins is better preserved.
- 3) The reconstruction is less noisy.

However, the convolutional reconstruction has better contrast and sharper definition of the "avenues" between fuel pins. Both reconstructions show a cupping density at the center of the bundle. This is probably due to a combination of film nonlinearities and beam hardening.

## VIII. SPECIFICATIONS OF THE INDUSTRIAL TOMOGRAPHIC SYSTEM

The tomographic scanner hardware is designed as a modular system. The source, scanner, and detector are each separate mechanisms mounted on a common stand as shown in Fig. 14. In this way, the system can be tailored to permit sensitivity and/or spatial resolution to be optimized for a particular problem. A laser is used for source-detector alignment.

A schematic of the detector collimator consists of a pair of movable plates permitting the collimator aperture to vary from a minimum of 0.1 mm up to a maximum of several millimeters on a side. The detector itself is simply placed behind the plates and can be a solid-state detector, a NaI detector, or a proportional counter depending upon the application. Of course, separate bulk shielding may be necessary to shield the detector from stray, scattered radiation.

The scanner assembly moves the object under inspection back and forth through the radiation beam and angularly rotates it between scans. The assembly is built from commercially available linear and rotational modules. The total linear travel is about 75 cm horizontally and has a vertical precision of 0.15 mm. The rotary motion is continuous with an angular precision of 0.02 degrees. All axes are driven by direct current stepping motors controlled by the LSI-11.

The source module is a table that permits any type of source to be mounted with it. Isotopic sources are inserted inside a cylindrical shield with an insert that collimates the beam to a cone with a 2-cm-diam base at the detector collimator. If the source detector distance is changed from the nominal 0.6 m, the source collimator insert may be changed to maintain the 2-cm-diam base.

All three modules are mounted on a stand that permits the source (x,y) detector modules to be moved along the beam axis. In this manner, we have the greatest flexibility in adjusting the various tomographic parameters.

The tomographic system interface controller that connects the LSI-11 computer to the mechanical tomographic scanner assembly is also designed in a modular fashion. This permits a high degree of flexibility and ease of modification for particular applications. A block diagram and photo of the controller is shown in Fig. 15. The connection to the LSI-11 can be via a standard DEC DR11C equivalent device interface card that allows parallel transfer of 16-bit words in or out. The projection data is recorded on floppy disks for later reconstruction. Then the system is accessed via a TI-700 terminal. To accommodate special radiation sources, such as the LASL 24-MeV betatron, it will only be necessary to transport the system to that source.

The interface logic chassis is organized around a bus concept with eight card slots. Any of these slots can be used for either positioning electronics or data-acquisition modules. When fully operational, up to eight detectors will be multiplexed per card slot. This will permit a detector arrangement amenable to a fan-beam geometry. This will facilitate more rapid projection gathering. A positioning module permits one to control a single mechanical motion with a stepping motor. Provisions are made for reading the absolute position from encoders, controlling speed via software over a 100 to 1 range with a stability of 0.01%, controlling acceleration and deceleration of the motor, detecting limit switch closures, and generating interrupts or start data-take signals at increments from 1 to 511 motor steps. Initially we are controlling two translational axes of motion and one rotational axis. In the future if it were desired to position very large assemblies, it is possible to use the same system with electrohydraulic stepping motors that are available in multihorsepower sizes.

The data-acquisition modules are designed with up to eight analog channels multiplexed into a single analog-to-digital converter. Conversely, it can also be used with a single analog-to-digital converter on each card. Initially a single 12-bit analog-to-digital converter with 40- $\mu$ sec minimum digitizing time is used to record x-ray transmission through the object being scanned. In normal operation the detector current is integrated between data takes. The end of conversion signal from the analog-to-digital converter is programmed to generate a computer interrupt. The provision for multiple inputs to a single analog-to-digital converter and for multiple data-acquisition modules will allow the use of a multidetector system. This will reduce the scan time required.

Most of the interface electronics is implemented with standard low-power Schottky TTL integrated circuits built on plug-in wire wrap cards. It fills about a half-rack of space. Most of this space is used for power supplies and the stepping motor power drivers. A local control panel on the interface allows positioning the system for initial scan setup and local troubleshooting.

## IX. EXPERIMENTAL RESULTS USING AN ELECTRONIC DETECTOR

This section will deal with several experiments conducted using a sodium iodide crystal and PMT tube combination as an x-ray or gamma-ray detector. The examples discussed involve reconstructions of actual reactor components or



phantoms that serve as mock-ups for reactor elements. The detector was operated as a current integrator.

Reconstruction was undertaken using either a conventional x-ray tube or a 100 curies of iridium 192 as a source. In the experiments to follow, we attempted to adhere to a 1% sensitivity criterion for shot material pathlengths. That is, if  $I$  is the number of detected photons at a projection point and  $I$  is Poisson distributed, then  $\sqrt{I}$  represents the estimated standard deviation or noise on the signal. The ratio of  $1/\sqrt{I}$  is equal to 1%. As mentioned earlier, these experiments all used the electronic detector in the current integration mode. However, the noise present in the projection data still follows an approximately Poisson distribution. It is expected that the above stated sensitivity criteria was violated when projections were gathered through the longer pathlengths present in a given object. We attempted to meet the 1% criteria on pathlengths that represented minimum path lengths through the object. Experimentally this involved the computation of a signal variance through a shot pathlength of the object. The integrator was adjusted until this variance fell below 1% of the mean detector output. This experimental trade-off was necessary in order to select a reasonable current integration time for each projection point.

The current integration time per point is also related to the number of source photons  $I_0$  emitted over the integration interval. The ratio of  $I/I_0$  (see Appendix A) represents the degree of source attenuation through various pathlengths in the object under study. It was mentioned earlier that a 12-bit linear A/D converter was used in these experiments. Thus, the numerical range of the intensity projection data was 0-4095. The dark current level, the level where the number of detected photons  $I$  fall to zero, was approximately 100. We adjusted the integrator on the detector so that the background A/D level, which measured the incident flux  $I_0$ , fell in a range above 3500. We concurrently set the minimum A/D level for longer pathlengths at or near 20. This would be 100 units above the dark current level. If one assumes the range is linear and near Poisson, the approximate  $I/I_0$  ratio would not be smaller than 3.5%. This corresponds to 15 db of source attenuation.

#### 1) Aluminum Disk

The initial reconstruction was undertaken using a 101.6-mm disk of aluminum. The primary reason for the test was to estimate density sensitivity of the prototype device under what could be considered nearly optimum conditions.

The source used was iridium. Six holes of 0.4, 0.762, 1.75, 3.81, 7.87, and 15.88-mm diam were drilled in the phantom. The scanning aperture was selected as 0.2 mm by 5 mm. The integration time per projection point was 100 ms. Figure 16a is the sinogram of the projections. For this example we used 360 projections at 1° increments with 512 points per projection. The reconstruction is shown in Fig. 16b.

We can clearly see all the holes down to 0.762 mm. We cannot, however, see the 0.4-mm-diam hole. We also noted that the holes were not reconstructed as circles. To date we have not discovered the reason for this. The problem was not noted in any later experiments. However, the primary purpose of this test was to discover the density sensitivity of an iridium source with a sodium-iodide detector. This was established since 0.762/101.6 corresponds to 0.75% density sensitivity. Based on the Nyquist criteria in the absence of noise, the theoretically highest sensitivity would be 0.4/101.6 or 0.4% based on a 0.2-mm scanning aperture. This result was encouraging since it verified that the detector circuitry was working at a higher level of sensitivity than the one to two percent minimum density sensitivity of radiographic film.

## 2) Small Reactor Pipe

The next experiment that we ran involved the detection of a small square machined thin region in a small stainless steel reactor pipe supplied by the Electric Power Research Institute (EPRI). The outside diameter of the pipe was 25.6 mm. The pipe wall was approximately 0.5 mm. The machine thinned spot was 150  $\mu$  on a side extending several millimeters down the length of the pipe. The scan aperture was chosen as 75  $\mu$  by 2 mm for this example. One hundred and eighty projections over 180° were collected with an integration time of 200 ms per projection point. Three hundred and eighty-four values were collected per projection.

Figures 17a and 17b represent sinograms of the projections. Figure 17a is a raw sinogram as scanned without beam-hardening correction. Figure 17b is the same sinogram as corrected. One should note the increased density differentials between the projected thin and thick material pathlengths in Fig. 17b. This indicates that the polynomial correction procedure is having the desired effect. Figure 18 is the reconstruction with correction through the plane of the groove. Note the small groove visible at 12 o'clock. It should be noted that this pipe was scanned using an x-ray source set at 150 keV and 1 mA.

### 3) Larger Reactor Pipe

The next example involves the reconstruction of an actual reactor pipe, supplied by Battelle-Northwest Laboratory. This pipe had been in a working reactor and had developed a corrosion pressure crack. The source used in this case was iridium. The outside diameter was 2.1 cm. The wall thickness was 1 mm. We used a 50- $\mu$  by 2-mm scanning aperture with 138 ms per projection point. One hundred and eighty projections with 512 points per projection were taken.

Beam-hardening correction was once again undertaken in this example. Figures 19a and 19b are the corresponding reconstructions. Note the decreased density differentials due to cupping in the pipe walls of Fig. 19b. This is the beneficial effect of beam correction. The 100- to 150- $\mu$  crack can clearly be seen at the 6:30 position.

### 4) Thoria Standard

The next test involved the scanning of a cylindrical fuel rod containing a cylindrical pellet of thorium with two machined dimples on its periphery. This standard was supplied by Bettis Atomic Power Laboratory. The standard itself consisted of a stainless steel cladding material 1.47 cm in outside diameter. The machined dimples protruded approximately 300  $\mu$  from the outer cylindrical boundary of the thorium pellet encased by the clad. The dimples extended no more than 1 mm down the outer side of the thorium wall. We decided on a scanning aperture of 50  $\mu$  by 1 mm for this test. Iridium was used as a source. There were 384 points per projection and 400 ms per projection point. One hundred eighty such projections were taken. Since there were no exterior markings on the clad to indicate a tomographic plane where dimples could be isolated, the correct tomographic plane was determined by experimentation. The results of the test are shown in Figs. 20a and 20b. Figure 20a is the reconstruction. It is immediately obvious that the thorium pellet is off-center relative to the clad. Also, it should be noted that the cupping artifact due to beam hardening is present. As mentioned earlier, multimaterial hardening is more difficult to accomplish and was not attempted.

The dimples were not obviously visible. However, Fig. 20b is another more extreme density stretch of Fig. 20a. A dimple is now visible at 8:30 o'clock.

### 5) Zirconium and Hafnium Standard

Our last test involved tomography of a rectangular phantom supplied by Bettis Atomic Power Laboratory. This was our initial test involving a test

object with two unequally dense objects. The test piece consisted of three small hafnium strips embedded in a matrix of zirconium. This test piece was scanned with an iridium source at 360, 1°-intervals. The scan aperture was 200  $\mu$  by 2 mm with a scan time per projection point of 200 ms. Figure 21 is the resulting sinogram. It shows the rotational effects as the three more-dense hafnium strips rotate into one indistinguishable mass. Note the increasing density as the piece rotates into and away from 135- and 315°-ranges. Figure 22a is a reconstruction of the data in Fig. 21. Note the obvious streaking artifacts caused by a loss of sensitivity and beam hardening. Figure 22b is a density thresholded version of Fig. 22a. Note that it is possible to isolate the small rectangular hafnium strips with relatively few artifacts. This thresholding capability could make the N-material hardening correction process possible, as outlined earlier.

#### X. CONCLUDING REMARKS

The Los Alamos Laboratory has undertaken a modest effort designed to apply computed tomography to nonmedical applications. Our limited experience indicates that potential users of this technology are hesitant to make large commitments of resources necessary to apply this technology to their problems without initial proof of concept experiments.

We have instituted a research plan designed to provide this information. Computer simulations provide the initial evidence that a task is feasible. This information is then used to configure the prototype scanner to perform the actual experiment. The flexible nature of the prototype makes this possible. Radiation sources from 30 pKv through 24 MeV may be used when necessary. Once feasibility has been established, we plan to aid the customer in the specification of a system for his production-oriented inspection task. Initial tests of the prototype have, for the most part, been successful.

In the near future we will experiment with cobalt and cesium as alternative radiation sources. We also hope to modify the detector electronics to accomplish photon counting in addition to the presently used current integration. Our staff hopes to construct a fan-beam detector array to speed up the projection-gathering process. These enhancements plus a multimaterial beam-hardening correction process should greatly increase the utility of this technology for NDE applications.

## REFERENCES

1. R. A. Crowther, D. J. DeRosier, and A. Klug, "The Reconstruction of a Three-Dimensional Structure from Projections and Its Application to Electron Microscopy," Proc. Roy. Soc. London A317 (1970) 319-340.
2. R. N. Bracewell and A. C. Riddle, "Inversion of Fan Beam Scans in Radio Astronomy," The Astrophys. J. 15 (1967) 427-438.
3. D. E. Kuhl and R. Q. Edwards, "Reorganizing Data from Transverse Section Scans of the Brain Using Digital Processing," Radiology 91 (1968) 975-983.
4. G. N. Hounsfield, "A Method of and Apparatus for Examination of a Body by Radiation Such as X or Gamma Radiation," Canadian Patent Specification No. 887891 (December 7, 1971).
5. Z. H. Cho, J. K. Chan, E. L. Hall, R. P. Kruger, D. G. McCaughey, "A Comparative Study of 3-D Image Reconstruction Algorithms with Reference to Number of Projections and Noise Filtering," IEEE Trans. on Nuc. Sciences, February 1975.
6. G. N. Ramachandran and A. V. Lakshminarayann, "Three-Dimensional Reconstruction from Radiographs and Electron Micrographs III, Description and Application of the Convolution Method," Indian J. Pure Appl. Phys. 9 (1971) 997-1003.
7. G. T. Herman and H. K. Liu, "Dynamic Boundary Surface Detection," Proc. 3rd Int. Conf. on Pattern Recognition (November 1976) 27-32.
8. R. P. Kruger and T. M. Cannon, "The Application of Computed Tomography, Boundary Detection and Shaded Graphics Reconstruction to Industrial Inspection," Mater. Eval. Vol. 36, No. 5, April 1978, 75-80.
9. R. P. Kruger, T. M. Cannon, A. S. Lundy, R. A. Morris, "Simulation and Preliminary Performance Characteristics of a Computed Tomography Device for Industrial Applications," SPIE Vol. 155, Image Understanding Systems and Industrial Application, August 1978, 178-183.
10. R. P. Kruger and R. A. Morris, "Simulated Neutron Tomography for Nondestructive Assays," SPIE Vol. 182, Imaging Applications for Automated Industrial Inspection and Assembly, 1979.
11. I. L. Morgan, H. Ellinger, R. Klinksiek, "Tomographic Analysis of Structural Materials," op. cit. Ref. 10.
12. C. F. Barton, K. Bailey, J. P. Barton, "Computerized Tomography for Industrial Applications," ASNT Spring Conf. Display, April 2-5, 1979, San Diego, California.
13. R. Gordon, "A Tutorial on ART," IEEE Trans. on Nucl. Sci. 21, No. 2 (1974) 78-93.

14. G. N. Minerbo, J. G. Sanderson, D. B. vanHulsteyn, P. Lee, "Three-Dimensional Reconstruction of X-ray Emission in Laser Imploded Targets," accepted for publication in Applied Optics.
15. J. Radon, "Über die Bestimmung von Funktion durch ihre Integralwerte largs Gewisser Mannigfaltigkeiten," Berichte Saechsische Akademie der Wessenschatten, 69 (1917) 262.
16. L. Wang, "Cross Section Reconstruction with a Fan-Beam Scanning Geometry," IEEE Trans. on Comp., Vol. C-26 (March 1977) 264-268.
17. B.K.P. Horn, "Density Reconstruction Using Arbitrary Ray-Sampling Schemes," Proc. of IEEE, Vol. 66, No. 5 (May 1978) 551-562.
18. E. L. Hall, Computer-Image Processing and Recognition (Academic Press, 1979) Chap. 5, 302.
19. K. M. Hanson and D. P. Boyd, "The Characteristics of Computed Tomographic Reconstruction Noise and Their Effect on Detectability," IEEE Trans. Nucl. Sci. NS-25 (February 1978) 160-163.
20. K. M. Hanson, "Detectability in the Presence of Computed Tomographic Reconstruction Noise," Proc. SPIE 127, Medicine IV (1978) 304-312.
21. Gerald Minerbo, "Maximum Entropy Reconstructions from Cone-Beam Projection Data," Comput. Biol. Med. Vol. 9, 1979, pp 29-37.
22. O. Nalcioglu, "Review of Beam Hardening Correction Methods in Computerized Tomography," Workshop on Transmission and Emission Computed Tomography, Seoul, Korea (1978).

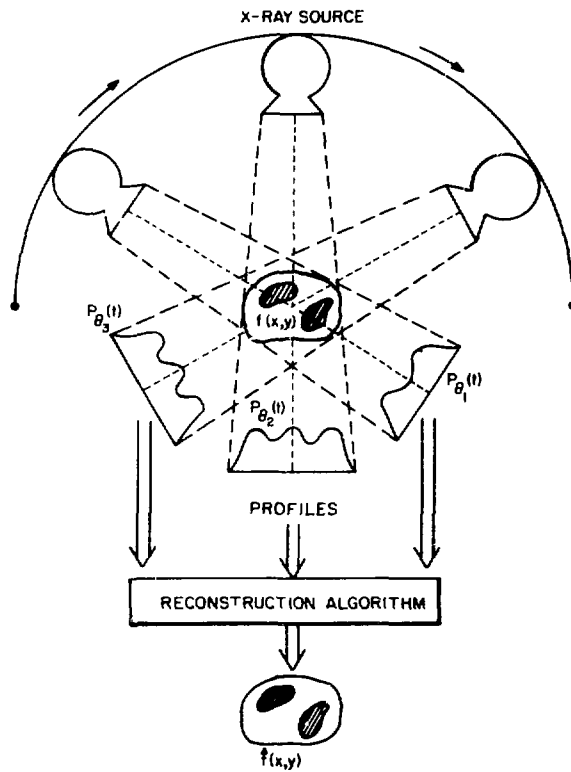


Fig. 1. Typical tomographic configuration.

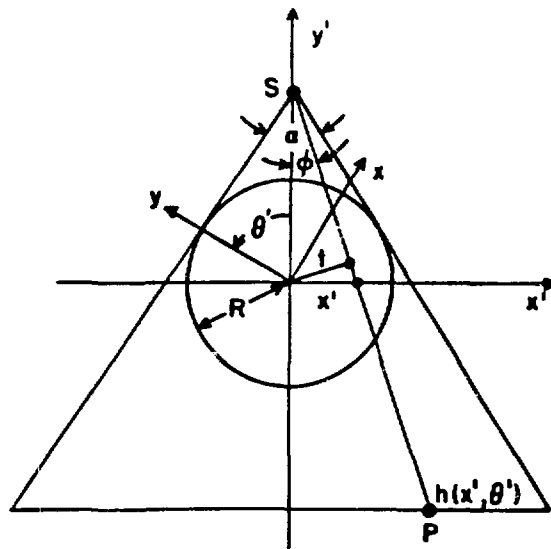


Fig. 2. Fan beam geometry.

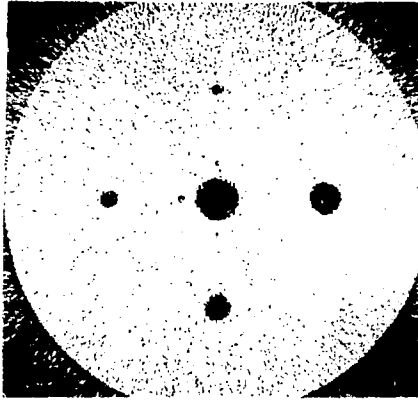


Fig. 3a. Plutonium simulation  
SNR = 4.

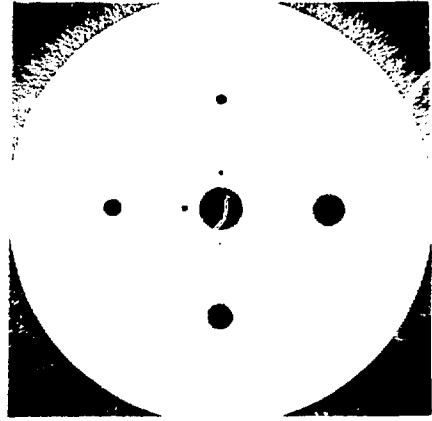


Fig. 3b. Plutonium simulation  
SNR = 10.

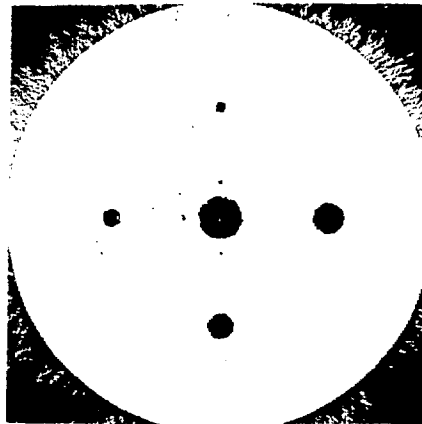


Fig. 3c. Plutonium simulation SNR = 4, reconstructed  
from fan beam data with  $\alpha = 76^\circ$ .

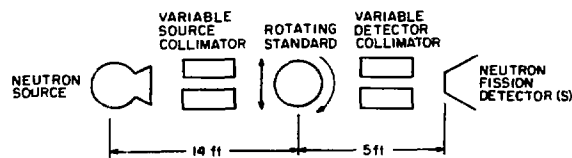


Fig. 4. NBS experimental configuration.



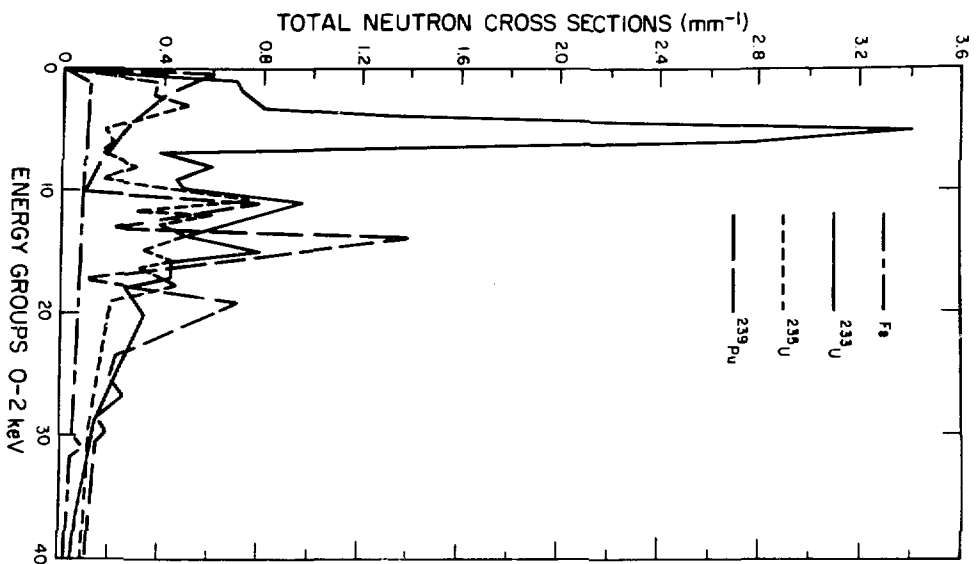


Fig. 5. Total neutron cross sections.

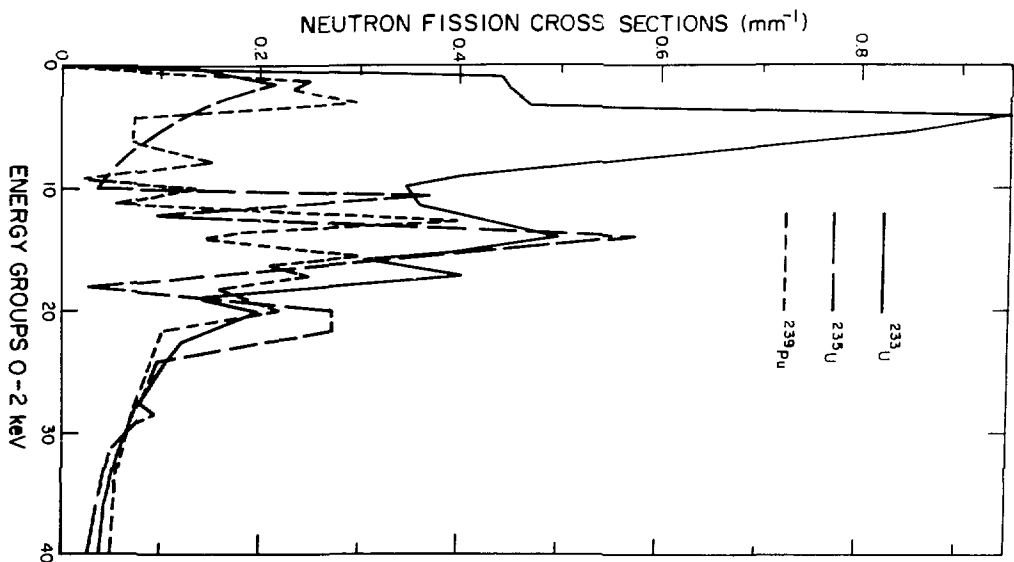


Fig. 6. Neutron fission cross sections for detectors.

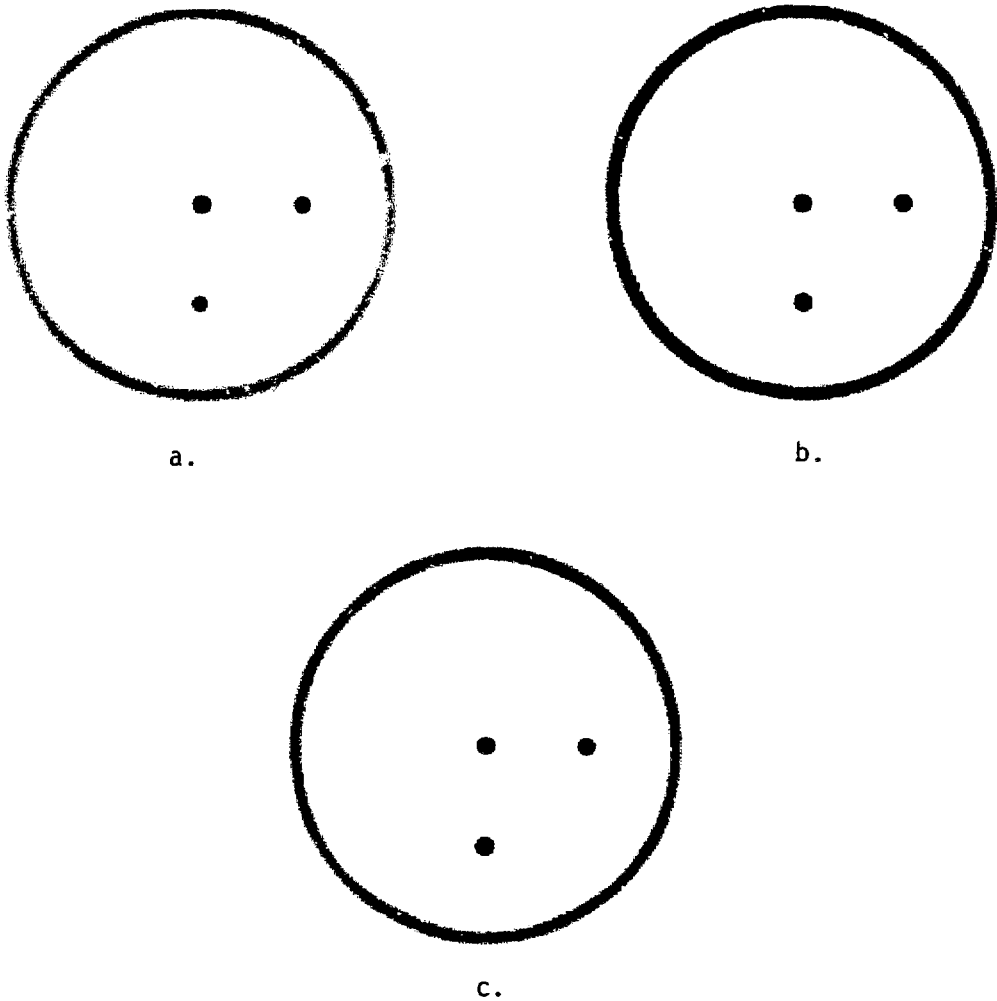


Fig. 7. Reconstructions with neutron detectors.

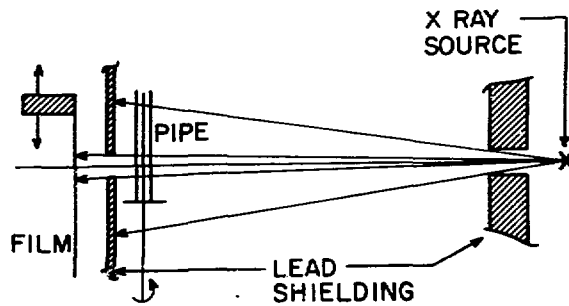


Fig. 8. Slit aperture, rotation, and x-y stage used in film tomography.

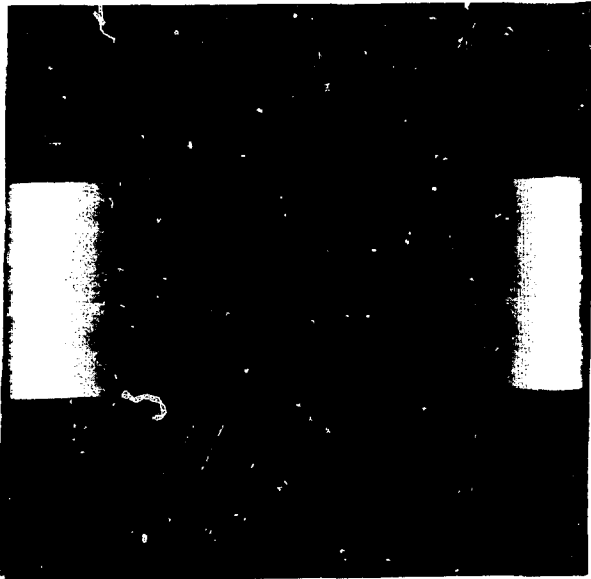


Fig. 9. Sinogram of reactor pipe.

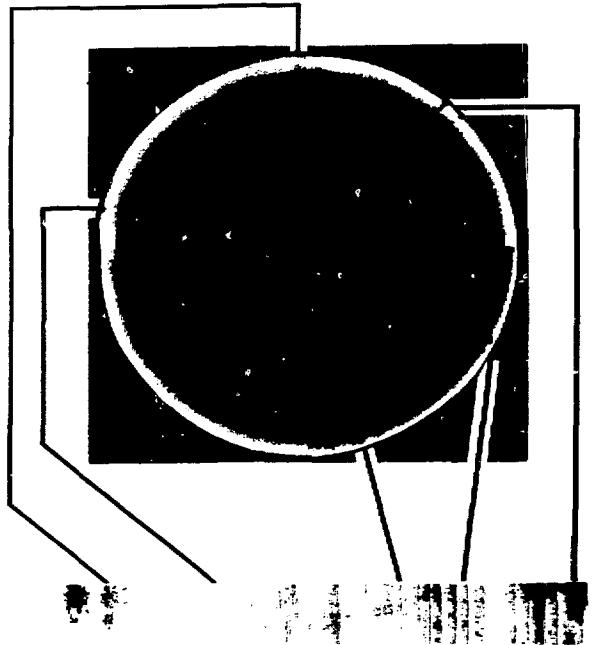


Fig. 10. Tomographic reconstruction of pipe and associated surface mosaic.



Fig. 11. Transmission neutron radiographs at 0°, 30°, and 60°.

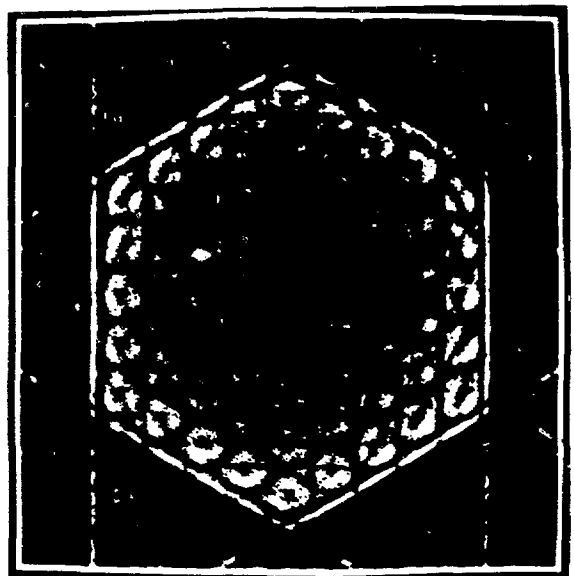


Fig. 12. Plane 6 reconstructed using backprojection.

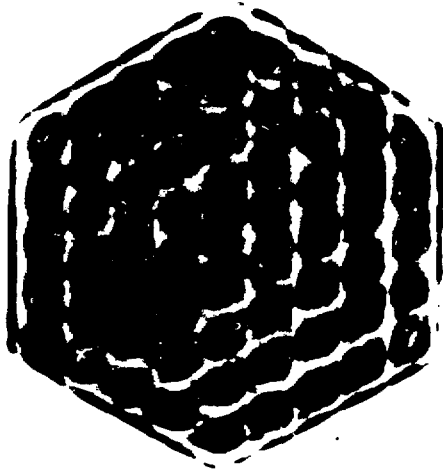


Fig. 13. Maximum entropy reconstruction of plane 6.



Fig. 14. Mechanical aspects of the tomographic prototype.

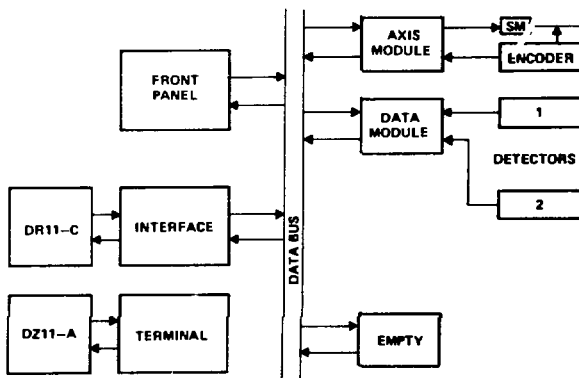


Fig. 15a. Schematic of prototype controller.

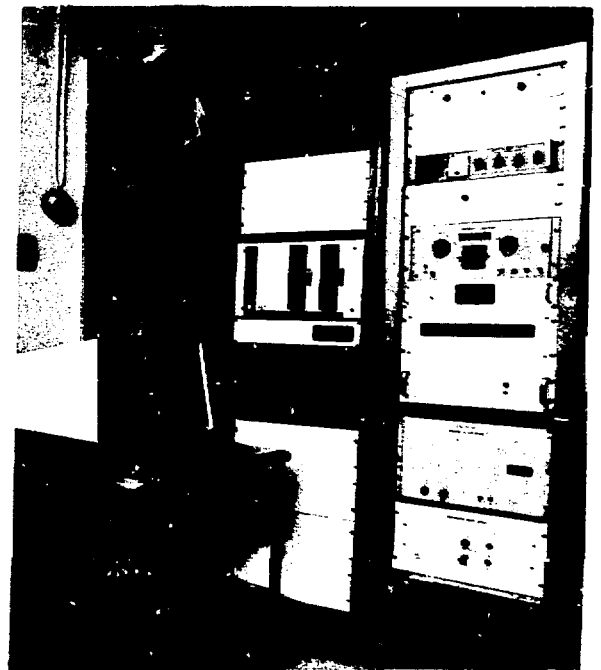


Fig. 15b. Photograph of prototype controller.

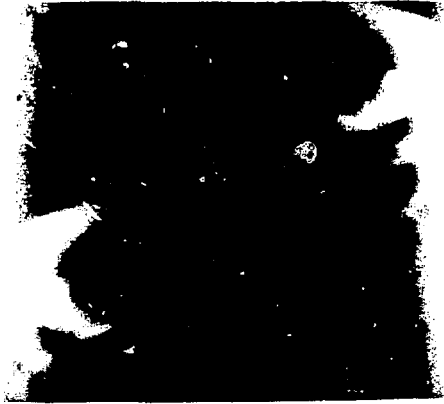


Fig. 16a. 180° sinogram of disk.

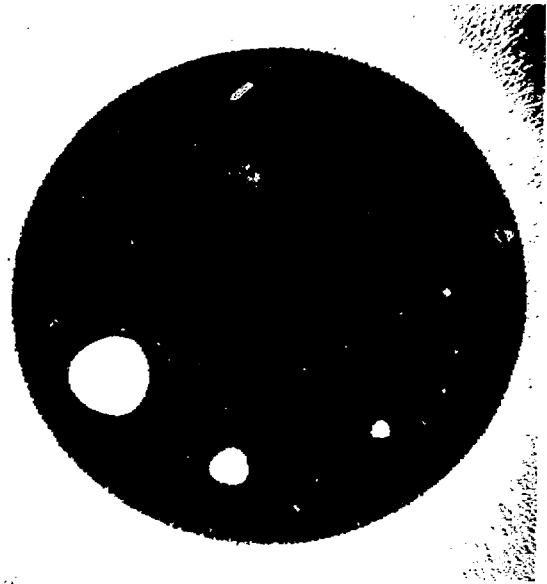


Fig. 16b. Reconstruction of aluminum disk.

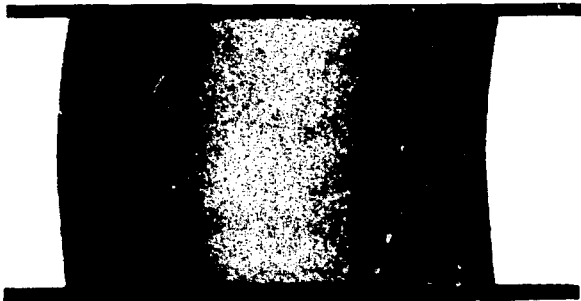


Fig. 17a. Sinogram of EPRI pipe prior to beam-hardening correction.

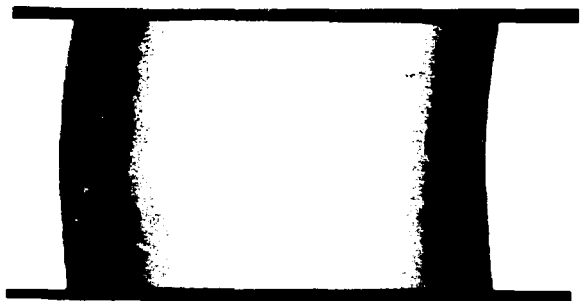


Fig. 17b. Sinogram of EPRI pipe after beam-hardening correction.



Fig. 18. Reconstruction with beam-hardening correction.

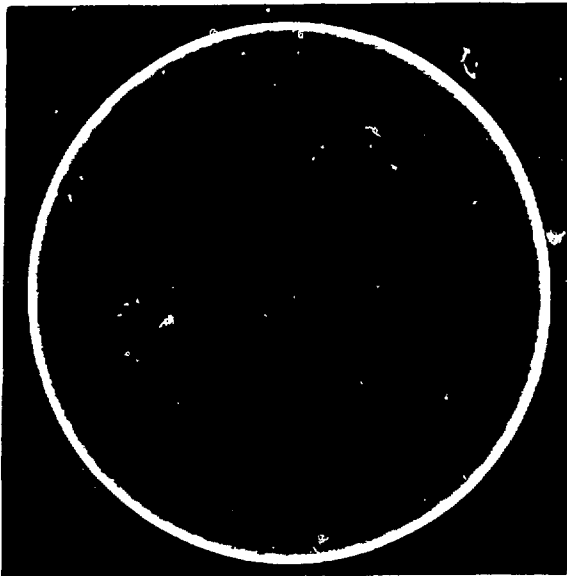


Fig. 19a. Reconstruction without beam-hardening correction.

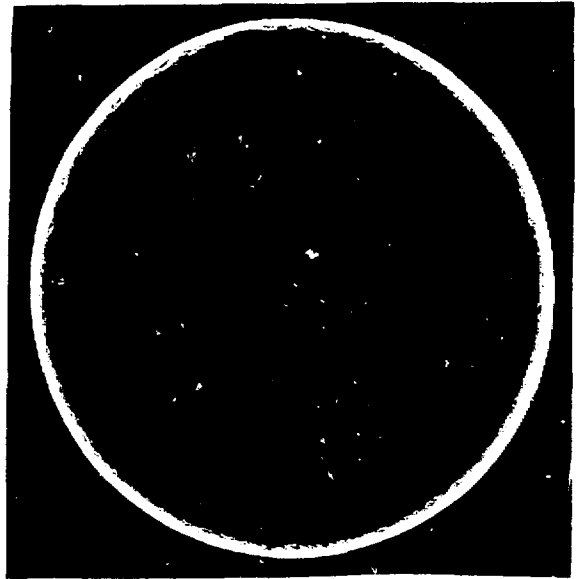


Fig. 19b. Reconstruction with beam-hardening correction.

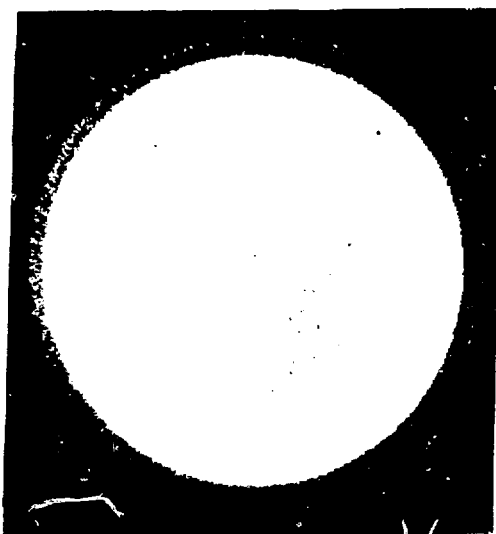


Fig. 20a. Thoria standard reconstruction.

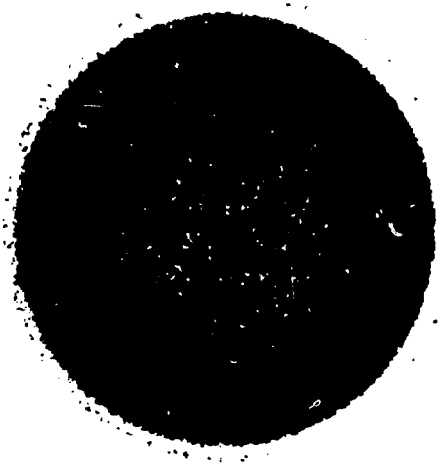


Fig. 20b. More extreme density stretched version of Fig. 20a.

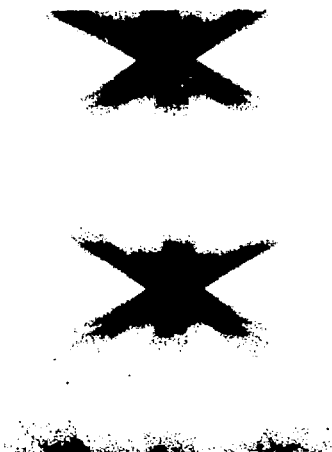


Fig. 21. Sinogram of rectangular test piece.

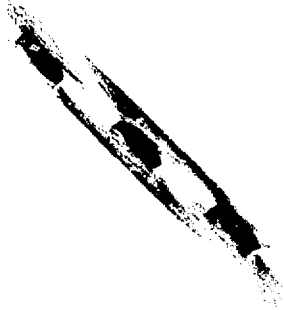


Fig. 22a. Reconstruction of two-material test piece.

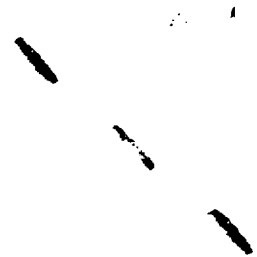


Fig. 22b. Density slicing to isolate hafnium in the test piece.

## APPENDIX A

### DERIVATION OF POISSON STATISTICS

We detect the ratio  $I/I_0$ , where  $I$  and  $I_0$  denote, respectively, the number of exit and incident photons. Thus, we estimate the line integral  $p$  by

$$p = -\ln(I/I_0) \quad . \quad (A1)$$

Here  $I$  is Poisson distributed with mean  $n$  and variance  $\sigma_n^2 = n$ . We linearize Eq. (A1) about the mean  $n$  by

$$p - \bar{p} = \left[ \frac{dp}{dI} \right]_{I=n} \cdot (I - n) = -\frac{1}{n} (I - n) \quad . \quad (A2)$$



This implies

$$E(p) = \bar{p} \quad , \quad (A3)$$

and

$$\sigma_p^2 = E \left[ (p - \bar{p})^2 \right] = \frac{1}{n} = e^{\bar{p}}/I_0 \quad . \quad (A4)$$

## APPENDIX B

### NEUTRON NOISE SIMULATION

Let  $I$  denote the number of detected neutrons (or photons). Assume  $I$  is Poisson distributed from the main text, Eq. (24) reduces in form to

$$I_\theta = I_0 \cdot D_K e^{-\int \mu(x,y) dy} \quad , \quad (B1)$$

where  $I_0$  is the total number of neutrons in the source overall energies  $L$ .  $D_K$  is the integrated detector response. Now

$$I'_\theta = \sigma^2(I) = E(I) \quad , \quad (B2)$$

where the noisy intensity  $I'_\theta$  is defined

$$I'_\theta = I_\theta + (I_\theta)^{1/2} \cdot \eta \quad , \quad (B3)$$

and  $\eta$  is Gaussian white noise.

It is the noisy estimate  $I'_\theta$  that is converted to total neutron pathlength in Eq. (26) of the main text.